A novel feedforward extended model reference adaptive control of PKMs: Design and real-time experiments

Youcef Mohamed Fitas, Ahmed Chemori, Johann Lamaury, Thierry Roux

A Novel Feedforward Extended Model Reference Adaptive Control of PKMs: Design and Real-Time Experiments

Youcef Fitas[a,b,*], Ahmed Chemori[a], Johann Lamaury[b] and Thierry Roux[b]

[a]LIRMM, University of Montpellier, CNRS, Montpellier, France
[b]SYMETRIE, Nîmes, France

ARTICLE INFO

Keywords:
Model reference adaptive control
Parallel kinematic manipulators
Model-based control
Dynamic model
Stability analysis

ABSTRACT

This paper presents a novel approach for controlling parallel kinematic manipulators (PKMs) using a feedforward augmented model reference adaptive control (MRAC) scheme. The original direct MRAC approach lacks the knowledge of the dynamic model and does not ensure boundedness of the feedback gains. To overcome these limitations, our proposed approach incorporates a feedforward dynamic term to enhance the tracking performance, and a projection operator to guarantee the boundedness of the feedback gains. The proposed controller is validated through real-time experiments using a 6-degree-of-freedom (DOF) PKM, and is compared with the original direct MRAC and some state-of-the-art controllers in various scenarios, including nominal and robustness cases. The obtained experimental results demonstrate the superiority of the proposed approach in terms of trajectory tracking performances and adaptation efficiency.

1. Introduction

Due to their innovative design, parallel kinematic manipulators (PKMs) offer numerous advantages in comparison with their serial counterparts [1]. These benefits encompass remarkable precision, substantial velocity and acceleration capabilities, and a remarkable payload-to-weight ratio [1]. Consequently, they stand as an optimal choice for a variety of industrial applications, including machining [2], micro-positioning [3], and motion simulation [4]. Furthermore, they have garnered increasing interest within both scientific and industrial communities [5]. Topics of exploration may include mechanism optimization [6], kinematic and dynamic modeling [7], kinematic calibration [8], as well as control design [9, 10, 11].

However, the formulation of effective control schemes assumes paramount importance in the operation of PKMs, given their highly nonlinear dynamics, uncertainties, and the presence of time-varying parameters [12]. Additionally, certain PKMs might behave challenges due to actuation redundancy [13], and the closed kinematic chain structure can potentially raise singularity issues [14]. The combination of these factors renders the task of control design for PKMs notably intricate [15]. Besides, PKMs are usually used for some applications, where trajectory tracking with high precision and micrometer-scale positioning are highly required, making the design of an efficient controller strongly recommended [3].

The existing literature includes a wide range of proposed control solutions dedicated to PKMs, where many of them have been both applied and successfully tested. Some control methodologies, such as PID-based controllers [16], are designed without the necessity of the robot's dynamic model knowledge. These controllers mainly rely on joint measurements and are often considered as non-model-based control approaches. While PID-based feedback controllers can offer satisfactory tracking performance under typical operational conditions, they may encounter issues related to stability or tracking performance when faced with uncertainties or external disturbances. This prompted the development of advanced control techniques to enhance the tracking performance of PID controllers [17, 18, 19]. Furthermore, the constant feedback gains may be designed as nonlinear gains [20]. The application of variable nonlinear feedback gains has demonstrated superior tracking performance compared to their constant counterparts, thereby conferring better disturbance rejection capabilities [20]. To strengthen the robustness of non-model-based control strategies, the integration of robustness aspects has proven its utility in improving tracking performance, particularly in the presence of uncertainties and external disturbances [21]. As example, the formulation of the RISE (Robust Integral Sign of the Error) feedback control strategy [22], which can also be further enhanced by considering nonlinear feedback gains [23].

To counteract high non-linearities and dynamic effects, these non-model-based controllers can be enhanced by incorporating the robot's dynamic model. This model can be introduced through either a computed torque formulation [24] or a feedforward formulation [25, 26]. Nevertheless, the efficacy of the computed torque formulation can be diminished by internal disruptions, including measurement noises. Furthermore, the presence of the Jacobian matrix in the model compensation, makes control inputs theoretically infinite in the presence of singularities within the workspace [14]. The feedforward approach can provide better robustness by replacing measured signals with desired ones and segregating feedback gains from the dynamic compensation. However, it can also lead to poor performance due to a false compensation in the presence of large uncertainties or inaccurate modeling [27].

*Corresponding author.
youcef-mohamed.fitas@lirmm.fr (Y. Fitas)
ORCID(s):

The effectiveness of the computed torque formulation can be further enhanced by incorporating robustness control terms, such as first-order Sliding Mode Control (SMC) [28]. This controller is known for its robustness against uncertainties and external disturbances, achieved through the incorporation of a discontinuous term. However, it is worth noting that this discontinuous term may lead to a chattering phenomenon [29]. To mitigate this issue, an advanced approach known as higher-order sliding mode control, such as the super-twisting algorithm, can be adopted [27]. To address the convergence challenges associated with the first-order sliding mode control, a Terminal Sliding Mode Control (T-SMC) strategy [30] can be used. This approach ensures finite-time convergence, overcoming the asymptotic convergence limitations of the first-order sliding mode control.

The dynamic model of the controlled system may also be used to design optimal control schemes. These approaches have been developed from a dynamic optimization problem that allows to generate optimal control inputs. The basic approach of this class is the Linear Quadratic Regulator (LQR) [31]. This controller can be augmented by an estimation filter using a locally optimal estimation, the resulting controller is known as Linear Quadratic Gaussian (LQG) controller [32]. Besides, the idea behind Model Predictive Control (MPC) is to optimize future control inputs through a robot dynamic model-based predictor [33]. However, when dealing with nonlinear models, predictive control might need a significant amount of computation burden.

An alternative approach to address the issue of large uncertainties is to design adaptive control schemes [34]. The objective here is to render the controller capable of adapting itself to variations within the system and its environment. This target can be accomplished by estimating the dynamic parameters and subsequently adapting the feedforward term [35]. The resulting design allows for real-time estimation and compensation of uncertainties. However, the process of adjusting the adaptation gains might need a significant amount of time. Additionally, for these controllers, the possibility of oscillations in the estimated parameters may appear for high adaptation gains, potentially leading to instability. Adaptive controllers can alternatively be developed without using the dynamic model. These controllers are designed especially in cases where obtaining or accurately characterizing the dynamic model is challenging. The objective behind this control design is to be adaptable to system variations and uncertainties without the need of estimating its parameters. One example of such design is Model Reference Adaptive Control (MRAC), which is based on stable reference model response [36]. The goal is to achieve the same behavior as a reference model. Another example is the L_1 Adaptive Control, which is an extension of MRAC including a state predictor and a low-pass filter applied to the control input [37]. Besides, neural networks can serve as potential tool for intelligent-based adaptive controllers [38, 39]. Their application holds particular significance in addressing uncertain nonlinear systems [38]. However, it is worth noting that such controllers may not account for the physical nature and structure of uncertainties and external disturbances.

Since MRAC is typically classified as a non-model-based control scheme, our approach seeks to harness the advantages of modeling and identification processes by computing a precise dynamic model. Accordingly, our study introduces a novel enhancement to the direct MRAC scheme through the incorporation of the robot's inverse dynamic model. This augmentation aims to design a comprehensive controller applicable to any PKM, while effectively compensating for the inherent dynamic effects in the control law. The resulting controller consists of two parts. The first one is a feedforward term derived from the robot's inverse dynamic model [36]. This term serves to compensate for high non-linearities and dynamic effects, thereby improving the tracking performance and adaptation efficiency. The second part is a non-model-based feedback term, characterized by adaptive feedback gains. These gains are designed to ensure a stable dynamic behavior aligned with a predefined reference model, to compensate for unmodeled phenomena, and residual errors. Additionally, the feedback gain adaptation laws are improved by incorporating a projection operator to prevent excessive gain values [37]. The main contributions of this paper are as follows:

- Design of a novel adaptive controller by integrating model-based feedforward compensation into MRAC control scheme.
- Enhanced adaptation mechanism by considering the projection operator, to ensure the boundedness of the feedback gains while guaranteeing fast adaptation.
- Exponential stability of the resulting closed-loop dynamics proved using Lyapunov arguments. The motivation behind this study is the novel design of the proposed controller, which incorporates a feedforward term and uses projection operators in one control solution.

As an application, and to demonstrate the efficiency and robustness of the proposed control scheme, it has been implemented through real-time experiments on a 6-DOF parallel kinematic manipulator (FOEHN robot). The rest of the paper is structured as follows. In Section 2, the structure along with the kinematic and dynamic modeling of the PKM testbed (FOEHN robot) are discussed. Section 3 provides a detailed presentation of the proposed control solution with a full stability analysis of the resulting closed-loop system. Section 4 presents the obtained experimental results. Finally, in Section 5, concluding remarks are provided, along with a discussion of potential future research directions.

2. Robot Description and Modeling

In this section, FOEHN parallel robot, a Gough-Stewart platform is described along with its mechanical structure. Then, its kinematic and dynamic models are detailed.

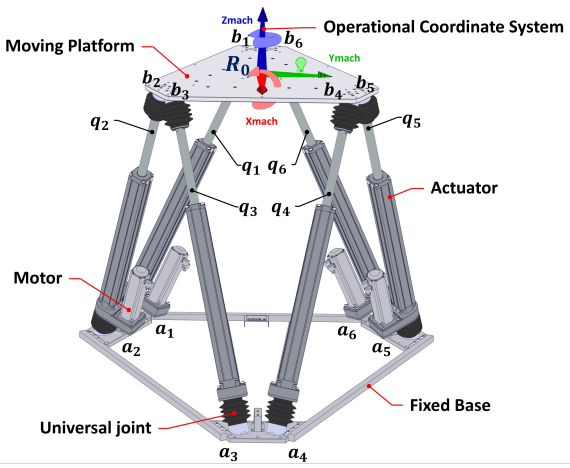

Figure 1: Virtual three-dimensional view of FOEHN 6-DOF parallel robot.

2.1. Robot description

A Gough-Stewart platform is a 6-DOF parallel kinematic manipulator, consisting of six independently actuated legs [40]. Its movement is generated by controlling the lengths of the six legs, allowing the moving platform of the robot to be manipulated. It offers several advantages, such as high accuracy, high repeatability and stiffness, making it a versatile tool for various applications, like motion simulation and micro-positioning [40].

FOEHN is a non-redundant Gough-Stewart platform, manufactured by the company SYMETRIE (cf. **Figure 1** for illustration). It is the R&D Hexapod of the company and is designed as a special version of the MISTRAL Hexapod. With a maximum payload capacity of 500 kg, FOEHN features six independently actuated legs powered by direct current (DC) motors.

2.2. Kinematics

The relationship between the joint and Cartesian coordinates is known as the kinematic model [41]. For the Gough-Stewart platform, this model gives the relationship between the lengths of the legs and the Cartesian coordinates of the moving platform. Let us consider a 6-DOF coordinate vector $\mathbf{x} = [x\ y\ z\ \phi\ \theta\ \psi]^T \in \mathbb{R}^6$ representing the position and orientation of the moving platform in the operational reference frame R_0 (see **Figure 1**). Also, let us consider another 6-DOF coordinate vector $\mathbf{q} = [q_1\ \cdots\ q_6]^T \in \mathbb{R}^6$ representing the lengths of the six legs. The six points $\mathbf{a_i}$, $i = 1, 2, ..., 6$ are the position coordinate vectors in the reference frame R_0 of the attachments between the fixed base and the robot legs. For the moving platform, the attachment points are represented by $\mathbf{b_i}$, $i = 1, 2, ..., 6$, which denote the position coordinate vectors of these points in the moving platform reference frame. The inverse kinematic model giving the vector $\mathbf{q}$ in terms of the vector $\mathbf{x}$ is expressed as follows [40]:

$$q_i = \|\mathbf{P} + \mathbf{R}\mathbf{b}_i - \mathbf{a}_i\|,\ i = 1, 2, ..., 6 \tag{1}$$

where $\mathbf{p} = [x\ y\ z]^T \in \mathbb{R}^3$ is the position of the moving platform in the operational reference frame. $\mathbf{R} \in \mathbb{R}^{3\times3}$ is its rotation matrix. The symbol $\|.\|$ denotes the standard Euclidean norm. Furthermore, for the description of the transformation between the joint and the Cartesian spaces velocities, the differential kinematic model can be used [5]. This model can be expressed as follows:

$$\dot{\mathbf{q}} = \mathbf{J}\dot{\mathbf{x}} \tag{2}$$

where $\dot{\mathbf{x}} \in \mathbb{R}^6$ is the vector of Cartesian velocities, $\dot{\mathbf{q}} \in \mathbb{R}^6$ is the vector of joint velocities and $\mathbf{J} \in \mathbb{R}^{6\times6}$ is the Jacobian matrix expressed by:

$$\mathbf{J} = \begin{bmatrix} \mathbf{s_1}^T & (\mathbf{R}\mathbf{b_1} \wedge \mathbf{s_1})^T \\ \vdots & \vdots \\ \mathbf{s_6}^T & (\mathbf{R}\mathbf{b_6} \wedge \mathbf{s_6})^T \end{bmatrix} \tag{3}$$

where $\mathbf{s_i} \in \mathbb{R}^3$, $i = 1, 2, ..., 6$ is the nominal vector associated to the i^{th} robot's leg, and the symbol $\wedge$ denotes the cross product of two vectors. This differential kinematic relationship is also used to convert the leg forces $\mathbf{f_l}$ into the forces and moments acting on the moving platform $\mathbf{f_p}$, through the Jacobian matrix as, $\mathbf{f_p} = \mathbf{J}^T\mathbf{f_l}$ [2]. In the case of PKMs, the forward kinematic model is often solved with numerical methods [42].

2.3. Dynamic model

In order to accurately describe the dynamics of FOEHN, a dynamic analysis is conducted using the Euler-Lagrange formulation. This analysis is formulated in both joint and mobile platform spaces, resulting in two separate dynamic equations, and it is compatible with many PKM architectures. The final dynamic model of the robot is obtained by combining these two dynamic equations. In order to reduce the complexity of the model, the following assumptions can be considered:

- ***Assumption 1***: The effects of elastic phenomena, at the leg and mobile platform levels, are neglected thanks to the materials used in the design.
- ***Assumption 2***: The passive universal joints of the robot are designed for optimal actuation performance, allowing to neglect the friction effects in these joints. For the active joints, both Coulomb and viscous friction effects are considered, as they are the most significant [43].
- ***Assumption 3***: Since the movements of the legs are slow compared to those of the mobile platform, and the actuation occurs at the leg level, their dynamics have been neglected.

The dynamic model of the platform represented as wrench vector $\mathbf{f_p}$ of the forces and moments applied by the legs onto the moving platform composed of (i) the inertial forces, (ii) the Coriolis and centrifugal forces, and (iii) the gravity vector:

$$\mathbf{f_p} = \mathbf{M_p}(\mathbf{x})\ddot{\mathbf{x}} + \mathbf{C_p}(\mathbf{x}, \dot{\mathbf{x}})\dot{\mathbf{x}} + \mathbf{G_p}(\mathbf{x}) \tag{4}$$

where $\mathbf{f_p}$ is the wrench vector of the legs acting on the platform, $\ddot{\mathbf{x}} \in \mathbb{R}^6$ is the Cartesian acceleration vector, $\mathbf{M_p(x)} \in \mathbb{R}^{6\times6}$ is the moving platform mass matrix, $\mathbf{C_p(x,\dot{x})} \in \mathbb{R}^{6\times6}$ is its Coriolis and centrifugal matrix, and $\mathbf{G_p(x)} \in \mathbb{R}^6$ is its gravitational force vector. The associated torque contribution of the resulting force $\mathbf{f_p}$, obtained using the Jacobian matrix, is expressed as follows:

$$\mathbf{\Gamma_p} = k_f \mathbf{J}^{-T} \left(\mathbf{M_p(x)}\ddot{\mathbf{x}} + \mathbf{C_p(x,\dot{x})}\dot{\mathbf{x}} + \mathbf{G_p(x)} \right) \tag{5}$$

where k_f is the conversion gain between the force applied by the leg and the motor torque. The actuator dynamic model can be expressed as follows:

$$\mathbf{\Gamma_m} = k_f \left(k_\alpha \mathbf{I_M}\ddot{\mathbf{q}} + \mathbf{F_v}\dot{\mathbf{q}} + \mathbf{F_s} sign(\dot{\mathbf{q}}) \right) \tag{6}$$

where $\ddot{\mathbf{q}} \in \mathbb{R}^6$ is the joint acceleration vector, $\mathbf{I_M} = I_m \mathbf{I_6} \in \mathbb{R}^{6\times6}$ is the actuator equivalent inertia matrix at the motor level, and the coefficients $\mathbf{F_v} = f_v \mathbf{I_6} \in \mathbb{R}^{6\times6}$ and $\mathbf{F_s} = f_s \mathbf{I_6} \in \mathbb{R}^{6\times6}$ represent the viscous and dry friction matrices, respectively. Finally, k_α is the conversion gain between the leg length and the motor angular position, and $\mathbf{I_6} \in \mathbb{R}^{6\times6}$ denotes the identity matrix. The resulting FOEHN complete inverse dynamic model, in the joint space, can be expressed as follows:

$$\mathbf{M(q)}\ddot{\mathbf{q}} + \mathbf{C}\left(\mathbf{q},\dot{\mathbf{q}}\right)\dot{\mathbf{q}} + \mathbf{G(q)} + \mathbf{\Gamma_f}(\dot{\mathbf{q}}) + \mathbf{\Gamma_d} = \mathbf{\Gamma} \tag{7}$$

where:

$$\begin{aligned}
\mathbf{M(q)} &= k_f \left(\mathbf{J}^{-T}\mathbf{M_p(x)}\mathbf{J}^{-1} + k_\alpha \mathbf{I_M} \right), \\
\mathbf{C(q,\dot{q})} &= k_f \mathbf{J}^{-T} \left(\mathbf{C_p(x,\dot{x})} - \mathbf{M_p(x)}\mathbf{J}^{-1}\dot{\mathbf{J}}\mathbf{J}^{-1} \right), \\
\mathbf{G(q)} &= k_f \mathbf{J}^{-T}\mathbf{G_p(x)}, \\
\mathbf{\Gamma_f}(\dot{\mathbf{q}}) &= k_f \left(\mathbf{F_v}\dot{\mathbf{q}} + \mathbf{F_s} sign(\dot{\mathbf{q}}) \right),
\end{aligned}$$

$\mathbf{\Gamma_d} \in \mathbb{R}^6$ is the vector of external disturbances, uncertainties, and non-modeled phenomena, and $\mathbf{\Gamma} \in \mathbb{R}^6$ is the vector of control input torques. Besides, for the dynamic model of robotic manipulators, the following properties are considered:

- ***Property 1***: The inertia matrix $\mathbf{M(q)}$ is symmetric, positive-definite and satisfies the following bounds:

$$m_{min}\|\varrho\|^2 \leq \varrho^T \mathbf{M(q)}\varrho \leq m_{max}(\mathbf{q})\|\varrho\|^2, \forall \varrho \in \mathbb{R}^6 \tag{8}$$

  where m_{min} is a positive constant and $m_{max}(\mathbf{q}) \in \mathbb{R}$ is a positive non-decreasing function

- ***Property 2***: If $\mathbf{q}(t)$ and $\dot{\mathbf{q}}(t)$ are also bounded, then $\mathbf{C(q,\dot{q})}$, $\mathbf{G(q)}$ and $\mathbf{\Gamma_f}(\dot{\mathbf{q}})$ are also bounded. Moreover, the dynamic model elements are differentiable with respect to $\mathbf{q}(t)$ and $\dot{\mathbf{q}}(t)$, respectively.

- ***Property 3***: All the elements of the vector $\mathbf{\Gamma_d}$ are bounded, that is:

$$\|\mathbf{\Gamma_d}\| \leq d_{max} \tag{9}$$

  where d_{max} is a positive constant.

Table 1
Summary of FOEHN robot parameters.

Parameter	Description	Value
m_p	Moving platform mass	$66\,kg$
I_x	x axis moving platform inertia	$6.44\,kg.m^2$
I_y	y axis moving platform inertia	$6.44\,kg.m^2$
I_z	z axis moving platform inertia	$12.86\,kg.m^2$
I_m	Actuator inertia	$0.001018\,kg.m^2$
f_v	Viscous friction coefficient	$4.3283\,N.s/m$
f_s	Dry friction coefficient	$51.8714\,N$
k_f	Gain force to torque	$0.0037\,m$
k_α	Gain leg length to motor angle	$356.0472\,m^{-1}$

The FOEHN robot parameters are summarized in the **Table 1**. These parameters are determined using different procedures. The conversion gains are calculated mathematically using the characteristics of the robot components. The moving platform mass is measured experimentally, while its inertia is calculated by the material assignment functionality of the computer-aided design software SolidWorks. For this procedure, high fidelity in replicating the materials and components of the manufactured robot is ensured to achieve better calculation accuracy. Finally, the actuator dynamic parameters are obtained through an identification procedure [44]. For the identification procedure, the vector of dynamic parameters, as well as the regressor must be explicitly formulated from the robot's dynamic model. Then, an input/output database is generated through the execution of high-acceleration trajectories. The objective is to estimate the values of those parameters by the solution of an optimization problem [44].

3. Proposed Control Scheme

In this section, the proposed control solution with the full stability analysis of the resulting closed-loop system are detailed.

3.1. Motivation

The design of adaptive control schemes for Gough-Stewart platform can greatly enhance its performances [36]. This platform requires a high level of robustness and accuracy, especially in the presence of uncertainties and external disturbances [11]. Developing a non-model-based control scheme, such as model reference adaptive control (MRAC), can provide a relevant solution to this challenging problem [36]. MRAC is designed to adapt the controller to the changes in the system behavior or environment, without the need for estimating its dynamic parameters [37]. The direct MRAC approach involves defining a reference model to force the desired performances by adjusting the controller parameters. This design is capable of enforcing nonlinear systems to follow reference dynamics, even in the presence of uncertainties and external disturbances [37]. The direct MRAC law can be expressed as follows:

$$\Gamma = \mathbf{K_p}(t)\mathbf{e} + \mathbf{K_d}(t)\dot{\mathbf{e}} \tag{10}$$

with

$$\mathbf{e} = \mathbf{q_d} - \mathbf{q} \tag{11}$$

where $\mathbf{q_d} \in \mathbb{R}^6$ is the desired joint position vector, $\mathbf{K_p}(t)$ is the proportional adaptive feedback gain matrix, and $\mathbf{K_d}(t)$ is the derivative adaptive feedback gain matrix. Their adaptation rules are based on the following second order reference system:

$$\ddot{\mathbf{e}}_\mathbf{m}(t) + 2\xi\omega_0\dot{\mathbf{e}}_\mathbf{m}(t) + {\omega_0}^2\mathbf{e}_\mathbf{m}(t) = 0 \tag{12}$$

where $\mathbf{e_m}(t) \in \mathbb{R}^6$ is the reference tracking error vector, $\dot{\mathbf{e}}_\mathbf{m}(t) \in \mathbb{R}^6$ is its first time derivative, and $\ddot{\mathbf{e}}_\mathbf{m}(t) \in \mathbb{R}^6$ is its second time derivative. The reference system damping ratio ξ and natural frequency ω_0 are also important parameters that should be carefully tuned to achieve the desired dynamic for the trajectory tracking errors. In order to adapt the control gain matrices, the following positive-definite symmetric matrix is considered:

$$\mathbf{P} = \begin{bmatrix} \mathbf{P_1} & \mathbf{P_2} \\ \mathbf{P_2} & \mathbf{P_3} \end{bmatrix} \tag{13}$$

where $\mathbf{P} \in \mathbb{R}^{12\times12}$ is the solution of the following static Lyapunov equation:

$$\mathbf{PD} + \mathbf{D}^T\mathbf{P} + \mathbf{Q} = 0 \tag{14}$$

where $\mathbf{D} \in \mathbb{R}^{12\times12}$ is the state matrix of the reference system (12), and $\mathbf{Q} \in \mathbb{R}^{12\times12}$ is a diagonal positive-definite weight matrix, expressed as follows:

$$\mathbf{Q} = \begin{bmatrix} 2\mathbf{Q_1} & 0 \\ 0 & 2\mathbf{Q_2} \end{bmatrix} \tag{15}$$

where $\mathbf{Q_1}, \mathbf{Q_2} \in \mathbb{R}^6$ are two diagonal positive-definite matrices to be tuned. Consequently, the adaptation rules of $\mathbf{K_p}(t)$ and $\mathbf{K_d}(t)$ feedback gains are given as follows:

$$\dot{\mathbf{K}}_\mathbf{p} = \mathbf{\Pi_1}\mathbf{\Omega}\mathbf{e}^T(t) \tag{16}$$

$$\dot{\mathbf{K}}_\mathbf{d} = \mathbf{\Pi_2}\mathbf{\Omega}\dot{\mathbf{e}}^T(t) \tag{17}$$

where $\mathbf{\Pi_1}$ and $\mathbf{\Pi_2}$ are the positive adaptation gain matrices to be tuned, with $\mathbf{\Omega} = \mathbf{P_2}\mathbf{e}(t) + \mathbf{P_3}\dot{\mathbf{e}}(t)$ [36]. This control law is expected to improve the tracking performance compared to non adaptive controllers, such as the standard PD controller, and can provide further robustness against variations and uncertainties [36]. However, this design does not guarantee the boundedness of the feedback gains, which may lead to potential overshoots, oscillations, and even instability [37]. Additionally, for this kind of control schemes, the considered uncertainties and external disturbances are mainly of unknown structure, which may degrade the control performance.

3.2. Proposed controller: Feedforward Model Reference Adaptive Control (FF-MRAC)

Our study aims at proving the performance and stability of a MRAC-based control scheme, incorporating the robot's dynamic model as a feedforward term. The goal is then to leverage the knowledge of the dynamic model for improved performances [27]. The added feedforward term is derived from the inverse dynamic model of the robot, and has the ability to counteract the nonlinear dynamics, thereby improving the reactivity of the controller without introducing any measurement noise into the control loop [27]. To achieve this, the proposed control solution (FF-MRAC) can be structured as follows:

$$\mathbf{\Gamma} = \mathbf{K_p}(t)\mathbf{e} + \mathbf{K_d}(t)\dot{\mathbf{e}} + \mathbf{\Gamma_{ff}} \tag{18}$$

where $\mathbf{\Gamma_{ff}}$ is the feedforward term, given from (7) as follows:

$$\mathbf{\Gamma_{ff}} = \mathbf{M}(\mathbf{q_d})\ddot{\mathbf{q}}_\mathbf{d} + \mathbf{C}(\mathbf{q_d}, \dot{\mathbf{q}}_\mathbf{d})\dot{\mathbf{q}}_\mathbf{d} + \mathbf{G}(\mathbf{q_d}) + \mathbf{\Gamma_f}(\dot{\mathbf{q}}_\mathbf{d}) \tag{19}$$

Thanks to the quality of the developed dynamic model, which accounts for the majority of dynamic phenomena, the inclusion of this term in the control law can have the potential to enhance the tracking performance by compensating for high nonlinear dynamics [27]. This nominal term was implemented based on the dynamic model (7) and the nominal values of the dynamic parameters provided in **Table 1**. Furthermore, it also has the advantage of improving the adaptation effect. The idea is to limit the MRAC adaptation to react only for the residual errors between the desired and actual trajectories, unmodeled uncertainties, and some external disturbances [25]. As a result, the proposed controller will gain both the benefits of dynamic compensation and reference-model-based adaptation for uncertain nonlinear systems. Additionally, the adaptation laws presented in (16) and (17) can be further improved through the incorporation of a projection operator. This will ensure that the gains remain bounded and do not diverge, thereby maintaining the feedback gains ($\mathbf{K_p}$ and $\mathbf{K_d}$) within admissible ranges [37]. This will also provide the opportunity to increase the adaptation gains ($\mathbf{\Pi_1}$ and $\mathbf{\Pi_2}$), making the adaptive correction faster and increasing the robustness of the proposed adaptive controller [37]. The resulting adaptation laws for the feedback gains can be then expressed as follows:

$$\dot{\mathbf{K}}_\mathbf{p} = \mathbf{\Pi_1} Proj\left(\mathbf{K_p}, \mathbf{\Omega}\mathbf{e}^T(t)\right) \tag{20}$$

$$\dot{\mathbf{K}}_\mathbf{d} = \mathbf{\Pi_2} Proj\left(\mathbf{K_d}, \mathbf{\Omega}\dot{\mathbf{e}}^T(t)\right) \tag{21}$$

As the projection operator is used, the feedback gains should remain within their admissible limits. This constraint is guaranteed by considering a convex function to restrict the adaptive gains. For more details about this operator, the reader can refer to [45]. Consequently, two upper bounds are defined, namely K_{p_b} for the proportional gain matrix,

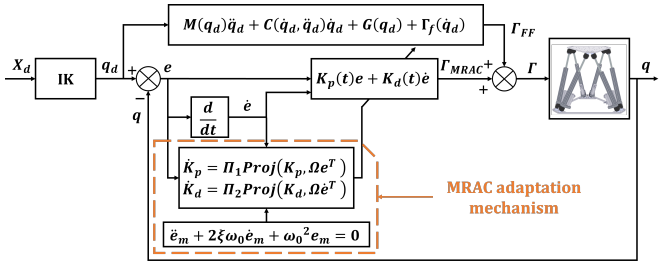

Figure 2: Block diagram of the proposed control solution.

and K_{db} for the derivative gain matrix [45]. This can be accomplished through the consideration of a smooth convex function to guarantee the limitation of the adaptive feedback gains. In our case, the smooth convex functions g_p and g_d are defined as:

$$g_p(\mathbf{K_p}) = \frac{(1+\beta)\|\mathbf{K_p}\|_F{}^2 - K_{pb}{}^2}{\beta K_{pb}{}^2} \tag{22}$$

$$g_d(\mathbf{K_d}) = \frac{(1+\beta)\|\mathbf{K_d}\|_F{}^2 - K_{db}{}^2}{\beta K_{db}{}^2} \tag{23}$$

where β is the projection tolerance bound to be tuned. Then, they should always satisfy the constraints $\|\mathbf{K_p}\|_F \leq K_{pb}, \|\mathbf{K_d}\|_F \leq K_{db}$, where $\|.\|_F$ denotes the Frobenius Euclidean norm. The block diagram of the proposed control scheme is depicted in **Figure 2**

3.3. Closed-loop stability analysis

The contribution of this paper includes the stability analysis of the resulting closed-loop system under the proposed control scheme. To this end, let us introduce the following theorem.

Theorem 1: The joint position tracking errors $e(t)$ of the robotic system whose dynamics is governed by (7), under the control law (18), where the feedback gains are adjusted with the adaptation rules (20), and (21), converge asymptotically to the origin.

Proof: To simplify the mathematical developments, let us first define the residual dynamics of robotic manipulators:

$$\begin{aligned}\mathbf{h}(\mathbf{q},\dot{\mathbf{q}}) &= \left[\mathbf{M}(\mathbf{q_d}) - \mathbf{M}(\mathbf{q})\right]\ddot{\mathbf{q}}_\mathbf{d} \\ &+ \left[\mathbf{C}\left(\mathbf{q_d},\dot{\mathbf{q}}_\mathbf{d}\right) - \mathbf{C}\left(\mathbf{q},\dot{\mathbf{q}}\right)\right]\dot{\mathbf{q}}_\mathbf{d} \\ &+ \left[\mathbf{G}(\mathbf{q_d}) + \mathbf{\Gamma_f}(\dot{\mathbf{q}}_\mathbf{d}) - \mathbf{G}(\mathbf{q}) - \mathbf{\Gamma_f}(\dot{\mathbf{q}})\right]\end{aligned} \tag{24}$$

Then, applying the control law in (18) to the robot's dynamic model (7) leads to:

$$\mathbf{M}(\mathbf{q})\ddot{\mathbf{e}} + \left(\mathbf{C}(\mathbf{q},\dot{\mathbf{q}}) + \mathbf{K_d}\right)\dot{\mathbf{e}} + \mathbf{K_p}\mathbf{e} + \mathbf{h}(\mathbf{q},\dot{\mathbf{q}}) - \mathbf{\Gamma_d} = 0 \tag{25}$$

By considering the reference model given in (12), and by taking $\mathbf{e_z} = \mathbf{e} - \mathbf{e_m} \in \mathbb{R}^6$, the following state-space model can be defined:

$$\dot{\hat{\mathbf{e}}}_\mathbf{z} = \mathbf{D}\hat{\mathbf{e}}_\mathbf{z} + \mathbf{B}\hat{\mathbf{e}}_\mathbf{m} + \delta \tag{26}$$

where $\hat{\mathbf{e}}_\mathbf{z} = [\mathbf{e_z}^T\ \dot{\mathbf{e}}_\mathbf{z}^T]^T \in \mathbb{R}^{12}$, and $\hat{\mathbf{e}}_\mathbf{m} = [\mathbf{e_m}^T\ \dot{\mathbf{e}}_\mathbf{m}^T]^T \in \mathbb{R}^{12}$. The state-space model matrices and the vector δ are given as follows:

$$\mathbf{D} = \begin{bmatrix} \mathbf{0_6} & \mathbf{I_6} \\ -\mathbf{D_1} & -\mathbf{D_2} \end{bmatrix},$$

$$\mathbf{B} = \begin{bmatrix} \mathbf{0_6} & \mathbf{0_6} \\ \mathbf{M(q)}^{-1}\mathbf{K_p} & \mathbf{M(q)}^{-1}\left(\mathbf{C(q,\dot{q})} + \mathbf{K_d}\right) \end{bmatrix},$$

$$\delta = \begin{bmatrix} \mathbf{0_6} \\ \mathbf{M(q)}^{-1}\left(\mathbf{h(q,\dot{q})} - \mathbf{\Gamma_d}\right) \end{bmatrix}$$

where $\mathbf{D_1} = \omega_0{}^2\mathbf{I_6} \in \mathbb{R}^{6\times6}$, $\mathbf{D_2} = 2\xi\omega_0\mathbf{I_6} \in \mathbb{R}^{6\times6}$, and $\mathbf{0_6} \in \mathbb{R}^{6\times6}$ is 6×6 matrix of zeros.

For the stability analysis of the resulting closed-loop system, let us consider the following positive-definite, radially unbounded, Lipschitz continuous Lyapunov candidate function:

$$V(\mathbf{y}) = \hat{\mathbf{e}}_\mathbf{z}^T\mathbf{P}\hat{\mathbf{e}}_\mathbf{z} + tr\left(\tilde{\mathbf{K}}_\mathbf{p}^T\tilde{\mathbf{K}}_\mathbf{p}\right) + tr\left(\tilde{\mathbf{K}}_\mathbf{d}^T\tilde{\mathbf{K}}_\mathbf{d}\right) \tag{27}$$

where $\mathbf{y} = \left[\hat{\mathbf{e}}_\mathbf{z}^T\ tr\left(\tilde{\mathbf{K}}_\mathbf{p}^T\tilde{\mathbf{K}}_\mathbf{p}\right)\ tr\left(\tilde{\mathbf{K}}_\mathbf{d}^T\tilde{\mathbf{K}}_\mathbf{d}\right)\right]^T \in \mathbb{R}^{2n+2}$, with $\tilde{\mathbf{K}}_\mathbf{p} = \mathbf{K_p}^* - \mathbf{K_p}$, and $\tilde{\mathbf{K}}_\mathbf{d} = \mathbf{K_d}^* - \mathbf{K_d}$, where $\mathbf{K_p}^*$ and $\mathbf{K_d}^*$ are the optimal proportional and derivative gains, respectively. This function $V(\mathbf{y})$ satisfies the following bounding inequality:

$$k_1\|\mathbf{y}\|^2 \leq V(\mathbf{y}) \leq k_2\|\mathbf{y}\|^2 \tag{28}$$

where $k_1 = min\{\lambda_{min}(\mathbf{P}), 1\}$ and $k_2 = max\{\lambda_{max}(\mathbf{P}), 1\}$, with $\lambda_{min}(.)$ and $\lambda_{max}(.)$ being the minimum and maximum eigenvalues of their arguments. Upon the use of the state-space model defined in (26), the adaptation laws (20)-(21), and the Lyapunov equation defined in (14), the first time-derivative of the Lyapunov function leads to the following:

$$\begin{aligned}\dot{V}(\mathbf{y}) = &-\hat{\mathbf{e}}_\mathbf{z}^T\mathbf{Q}\hat{\mathbf{e}}_\mathbf{z} - 2tr\left(\left(\tilde{\mathbf{K}}_\mathbf{p}\mathbf{\Pi}_1 - \mathbf{M(q)}^{-1}\mathbf{K_p}\right)\left(\mathbf{\Omega e}^T\right)\right) \\ &- 2tr\left(\left(\tilde{\mathbf{K}}_\mathbf{d}\mathbf{\Pi_2} - \mathbf{M(q)}^{-1}\left(\mathbf{C(q,\dot{q})} + \mathbf{K_d}\right)\right)\left(\mathbf{\Omega}\dot{\mathbf{e}}^T\right)\right) \\ &+ \hat{\mathbf{e}}_\mathbf{z}\mathbf{P}\delta\end{aligned} \tag{29}$$

Considering the dynamic model properties, and given that $\tilde{\mathbf{K}}_\mathbf{p} \leq \mathbf{K_p}^* + K_{pb}\mathbf{I_6}$ and $\tilde{\mathbf{K}}_\mathbf{d} \leq \mathbf{K_d}^* + K_{db}\mathbf{I_6}$, upon the use of (20) and (21), respectively. The function $\dot{V}(\mathbf{y})$ can be upper-bounded as follows:

$$\begin{aligned}\dot{V}(\mathbf{y}) \leq &-\lambda_{min}(\mathbf{Q})\|\hat{\mathbf{e}}_\mathbf{z}\|^2 \\ &- 2tr\left(\left(\left(\mathbf{K_p}^* + K_{pb}\mathbf{I_6}\right)\mathbf{\Pi_1} - \frac{K_{pb}}{m_{min}}\mathbf{I_6}\right)\left(\mathbf{\Omega e}^T\right)\right) \\ &-2tr\left(\left(\left(\mathbf{K_d}^* + K_{db}\mathbf{I_6}\right)\mathbf{\Pi}_2 - \frac{K_{cmax} + K_{db}}{m_{min}}\mathbf{I_6}\right)\left(\mathbf{\Omega}\dot{\mathbf{e}}^T\right)\right) \\ &+ \hat{\mathbf{e}}_\mathbf{z}\mathbf{P}\delta\end{aligned} \tag{30}$$

where $K_{cmax} = K_c\dot{q}_{max}$, and $\dot{q}_{max} = max\{\|\dot{\mathbf{q}}\|\}$, with K_c is positive constant. By selecting Π_1 and Π_2 such that $\left(\mathbf{K_p}^* + K_{pb}\mathbf{I_6}\right)\mathbf{\Pi_1} - \left(\frac{K_{pb}}{m_{min}} - 1\right)\mathbf{I_6} > 0$ and $\left(\mathbf{K_d}^* + K_{db}\mathbf{I_6}\right)\mathbf{\Pi_2} -$

$\left(\frac{K_{cmax}+K_{db}}{m_{min}} - 1\right)\mathbf{I_6} > 0$, the following matrices can be defined as follows:

$$\mathbf{\Upsilon_1} = \left(\mathbf{K_p}^* + K_{pb}\mathbf{I_6}\right)\mathbf{\Pi_1} - \frac{K_{pb}}{m_{min}}\mathbf{I_6} \tag{31}$$

$$\mathbf{\Upsilon}_2 = \left(\mathbf{K_d}^* + K_{db}\mathbf{I_6}\right)\mathbf{\Pi_2} - \frac{K_{cmax} + K_{db}}{m_{min}}\mathbf{I_6} \tag{32}$$

Then, considering the fact that the Euclidean norm of the residual dynamics can be upper bounded $\|\mathbf{h}(\mathbf{q}, \dot{\mathbf{q}})\| \leq K_{h_1}\|\dot{\mathbf{e}}\| + K_{h_2}\|\mathbf{e}\|$, and $\|\mathbf{\Gamma}_d\| \leq K_{h_3}\|\hat{\mathbf{e}}\|$, with K_{h_1}, K_{h_2} and K_{h_3} being three positive constants. The time-derivative of $V(\mathbf{y})$ can then be upper-bounded as follows:

$$\dot{V}(\mathbf{y}) \leq -\lambda_{min}(\mathbf{Q})\|\hat{\mathbf{e}}_z\|^2 - 2\epsilon\|\hat{\mathbf{e}}\|^2 + \lambda_{max}(\mathbf{P})K_h\|\hat{\mathbf{e}}_z\|\|\hat{\mathbf{e}}\| \tag{33}$$

where $\hat{\mathbf{e}} = [\mathbf{e}^T\ \dot{\mathbf{e}}^T]^T \in \mathbb{R}^{12}$, $K_h = max\{K_{h_1}, K_{h_2}\} + K_{h_3}$, and $\epsilon = \lambda_{min}(\mathbf{\Sigma})$, with $\mathbf{\Sigma}$ being a positive-definite symmetric matrix, defined as follows:

$$\mathbf{\Sigma} = \begin{bmatrix} \mathbf{P_2\Upsilon_1} & \mathbf{P_2} \\ \mathbf{P_3} & \mathbf{P_3\Upsilon_2} \end{bmatrix} \tag{34}$$

By computing the squares, the following upper-bound can be obtained:

$$\dot{V}(\mathbf{y}) \leq -\left(\lambda_{min}(\mathbf{Q}) - \frac{\lambda_{max}(\mathbf{P}){K_h}^2}{8\epsilon}\right)\|\hat{\mathbf{e}}_\mathbf{z}\|^2 \tag{35}$$

Designing the adequate reference system matrix $\mathbf{D}$, with adequate weighting matrix $\mathbf{Q}$, the following inequality can be deduced:

$$\lambda_{min}(\mathbf{Q}) - \frac{\lambda_{max}(\mathbf{P}){K_h}^2}{8\epsilon} > 0$$

which means that $\|\hat{\mathbf{e}}_z\|$ converges asymptotically to zero, thereby $\|\hat{\mathbf{e}}\|$ converges also to zero as $\hat{\mathbf{e}}_m$ has the behavior of a stable reference system (i.e. Hurwitz). Consequently, the tracking errors converge asymptotically to zero, and this concludes the proof.

4. Real-time Experimental Results

In this section, the efficiency and robustness of the proposed FF-MRAC control scheme is demonstrated through real-time experiments conducted on FOEHN parallel robot, a Gough-Stewart platform, described in Section 2.1. The objective is to showcase its high performance and superiority. For this purpose, the proposed controller is compared with MRAC-based adaptive control, and with two model-based controllers: The sliding mode controller (SMC) detailed in [28], and the augmented Feedforward PD (FF-PD) controller proposed in [43]. To validate the proposed control solution through real-time experiments, the following scenarios are considered:

- ***Scenario 1 – nominal case:*** The controllers are applied to FOEHN parallel robot under nominal conditions, without uncertainties nor external disturbances.
- ***Scenario 2 – robustness towards payload changes:*** To assess the robustness of the controllers, a series of tests are conducted with three distinct payloads individually fixed at the center of the mobile platform (cf. **Figure 3** for illustration). These payloads weight respectively $100\,kg$, $150\,kg$, and $200\,kg$.
- ***Scenario 3 – robustness towards velocity changes:*** The robustness of the controllers can also be tested by applying reference trajectories with higher velocities. Indeed, two high-velocity tests are proposed: the first one with a maximum joint velocity of $V_{max_1} = 310\,mm/s$, and a second with a maximum velocity of $V_{max_2} = 390\,mm/s$.

4.1. Experimental platform and some implementation issues

4.1.1. Experimental platform

The FOEHN parallel robot is equipped with high-dynamic brushless DC motors and absolute EnDat 2.2 encoders. The motors have a maximum torque of $18\,N.m$ and a maximum velocity of $3500\,rpm$. The encoders are used to measure the angular positions in real time and calculate the corresponding prismatic joint lengths. The motors are controlled by two multi-axis servo drives, each of them controlling three motors. The control torque inputs are sent to the drives from an OMRON CK3E controller with a servo cycle of $2\,kHz$ through an EtherCAT fieldbus. The controller consists of a two-core armv7l CPU with a clock frequency of $1\,GHz$. The servo control is designed in joint space with real-time prismatic joint length feedback. The controllers are implemented in Matlab/Simulink from MathWorks and then converted to C language. Finally, the code is compiled and uploaded into the CK3E controller. Since the servo cycle is set to $2\,kHz$, the CPU should perform the calculations and send the commands to the drives within $0.5\,ms$. If this time limit is exceeded, a safety mechanism activates to stop the robot and prevent potential damage. In order to avoid overshoots in the input torques for the sliding mode controller, the sign function was replaced by a smooth approximation based on the hyperbolic tangent function.

The parameters ξ and ω_0 of the reference model are determined based on its time performance specifications. These specifications are selected according to the type of the controlled system [46]. A maximum first overshoot of 5 % ($M_p = 5\,\%$) and a settling time of 0.2 seconds at 5 % ($t_{r_{5\%}} = 0.2\,s$) are used in our case. The other control parameters are experimentally tuned using the trial-and-error method. The adaptive gains are gradually increased to achieve a reactive adaptation, while carefully avoiding oscillations and excessive variation. Additionally, these gains are higher for the proposed controller, as the boundedness of the feedback gains is ensured through the use of projection operators. The results of this tuning are summarized in **Table 2**. The upper limits of the adaptive gains have been tuned to avoid vibrations and oscillations in the control signal. This tuning was performed for the nominal case, and the same limits

Figure 3: Illustrative views of the experimental setup of FOEHN parallel robot.

Table 2
Summary of the control design parameters.

MRAC	SMC	FFPD	FF-MRAC
$\mathbf{K_p}(0) = 8550\mathbf{I_6}$	$\mathbf{\Lambda} = 55\mathbf{I_6}$	$\mathbf{K_p} = 8550\mathbf{I_6}$	$\mathbf{K_p}(0) = 8550\mathbf{I_6}$
$\mathbf{K_d}(0) = 56.5\mathbf{I_6}$	$\mathbf{K_s} = 8.2\mathbf{I_6}$	$\mathbf{K_d} = 56.5\mathbf{I_6}$	$\mathbf{K_d}(0) = 56.5\mathbf{I_6}$
			$K_{pb} = 10920$
			$K_{db} = 68.25$
			$\beta = 0.1$
$\mathbf{Q_1} = 10\mathbf{I_6}$			$\mathbf{Q_1} = 10\mathbf{I_6}$
$\mathbf{Q_2} = 100I_6$			$\mathbf{Q_2} = 100\mathbf{I_6}$
$\mathbf{\Pi_1} = 100000I_6$			$\mathbf{\Pi_1} = 200000I_6$
$\mathbf{\Pi_2} = 0.15I_6$			$\mathbf{\Pi_2} = 0.5I_6$
$\xi = \frac{1}{\sqrt{2}}$			$\xi = \frac{1}{\sqrt{2}}$
$\omega_0 = 20\,rad/s$			$\omega_0 = 20\,rad/s$

were maintained for other scenarios to test the robustness of the proposed solution.

The desired trajectories are sent to the CK3E controller from the SYM_Motion software, a GUI developed by SYMETRIE. This software allows the creation, validation, and execution of multiple movement types and establishes communication with the controller through a TCP/IP Ethernet connection. It is worth noting that during the experimental validation, all the limits for the robot were respected. Furthermore, all singularities are located outside of the robot's workspace, thanks to the robot's mechanical design and the SYM_Motion software limitations.

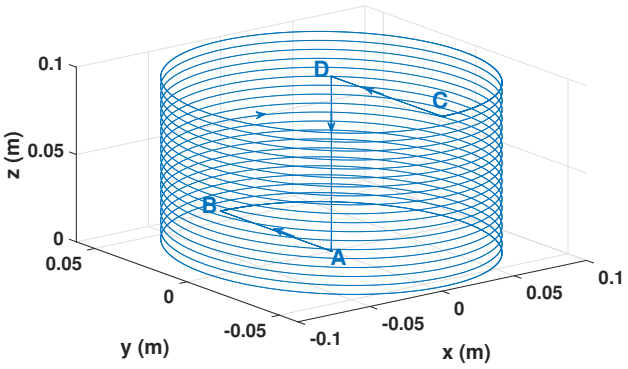

Figure 4: 3D-view of the elliptical cylinder-shaped reference trajectory A-B-C-D-A.

4.1.2. Trajectory generation and evaluation criteria

The desired trajectories are generated in the operational space using the SYM_Motion software. Consequently, these trajectories are designed to respect the robot's workspace constraints and avoid singularities. A 3D-view of the resulting trajectory is illustrated in **Figure 4**. As displayed, the moving platform undergoes a linear trajectory from point A ($0\,mm, 0\,mm, 0\,mm$) to point B ($0\,mm$, $60\,mm, 0\,mm$), followed by an elliptical trajectory leading to point C ($0\,mm, -60\,mm, 100\,mm$). It subsequently traverses point D ($0\,mm, 0\,mm, 100\,mm$) before retracing its path back to point A. For the rotational component, a sinusoidal trajectory is employed with an amplitude of 3° and a frequency of $0.3\,Hz$. A phase shift of 120° is maintained between the rotational angles. The total duration of the reference trajectory is of 50 seconds.

Regarding the scenario of robustness towards velocity changes, and in order to create high velocities in the joint space, an helicoidal trajectory is proposed, described by the following analytical expressions:

$$\begin{cases} x(t) = 0.02sin\,(2\pi f t) \\ y(t) = 0.02cos\,(2\pi f t) \\ z(t) = 0.01 - 0.02cos\left(\frac{2\pi f}{8} t\right) \\ \phi(t) = \frac{\pi}{60} sin\,(2\pi f t) \\ \theta(t) = \frac{\pi}{60} cos\,(2\pi f t) \\ \psi(t) = 0 \end{cases} \tag{36}$$

It is worth noting that the translations are expressed in meter and the rotations in radian. The frequency of the first test is chosen as $f = 1.3Hz$ and for the second one as $f = 1.6Hz$. The whole duration of the trajectory is of 60 seconds. Additionally, this trajectory is smoothed out at both the beginning and end with a 5 seconds fade period.

For the comparative analysis purpose, the evaluation of performance is established using quantitative metrics, based on the root mean square error (RMSE) for translation (RMS_t), rotation (RMS_r), and joint positions (RMS_q).

These criteria are mathematically expressed as follows:

$$RMS_t = \sqrt{\frac{1}{N}\sum_{i=1}^{N}\left({e_x}^2(i) + {e_y}^2(i) + {e_z}^2(i)\right)} \quad (37)$$

$$RMS_r = \sqrt{\frac{1}{N}\sum_{i=1}^{N}\left({e_\phi}^2(i) + {e_\theta}^2(i) + {e_\psi}^2(i)\right)} \quad (38)$$

$$RMS_q = \sqrt{\frac{1}{N}\sum_{i=1}^{N}\left(\sum_{j=1}^{6} e_{q_j}^2(i)\right)} \quad (39)$$

where e_x, e_y, e_z, e_ϕ, e_θ, and e_ψ are the Cartesian tracking errors, $e_{q_j}, j = 1, 2, ..., 6$ are the joint tracking errors and N is the total number of samples. It is worth noting that the Cartesian tracking errors are calculated from the measured joint ones using the forward kinematic model [5].

4.2. Experimental results

4.2.1. Scenario 1: Nominal case

The evolution versus time of the tracking errors is depicted in **Figures 5** and **6**, with a zoomed in plot between 30 and 35 seconds for a better readability. The proposed control solution enhances the tracking performance with respect to alternative controllers. When compared to MRAC, this improvement can be attributed to dynamic compensation, and the fast adaptation obtained thanks to the projection operators. Compared to SMC, the improvement arises from the adaptive design and the use of desired trajectories through the incorporation of a feedforward term. Despite the robust performance of SMC and its efficiency in translations, as shown in **Figure 6**, the proposed approach offers enhanced results. Besides, compared to the FF-PD controller, the improvement can be attributed to the adaptive feedback mechanism based on MRAC, where the proposed controller can be adjusted in real-time with its adaptive feedback gains, in contrast to the constant gains used in the FF-PD controller. Numerical calculation of the RMSE-based metrics confirms these improvements, as summarized in **Table 3**. The evolution of the adaptive feedback gains is depicted in **Figures 7** and **8**. The projection operator ensures the non-divergence of the adaptive feedback gains, unlike the original MRAC controller, thereby increasing the adaptation gains to improve the reactivity of the controller results in a more effective and precise control.

The generated control input torques, for the fourth controllers, are illustrated in **Figure 9** with a zoomed in plot within the range $[30\,s, 35\,s]$ for more readability. These torques remain in their admissible range, and since the SMC controller includes a discontinuous term, it leads to a chattering, even with the use of a hyperbolic tangent approximation to mitigate this effect.

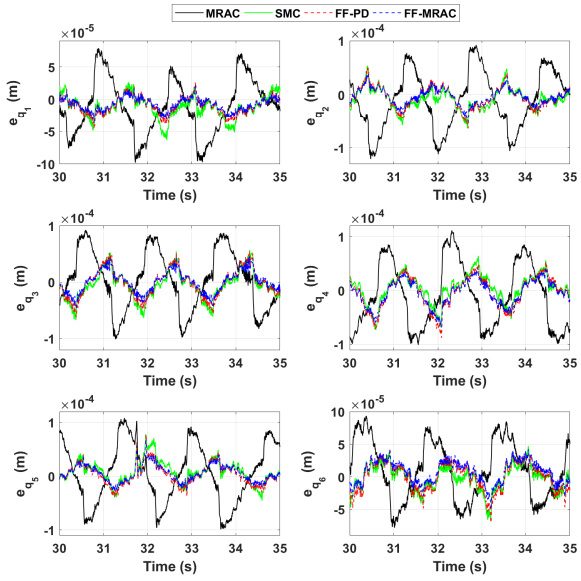

Figure 5: Evolution versus time of the joint tracking errors (Scenario 1).

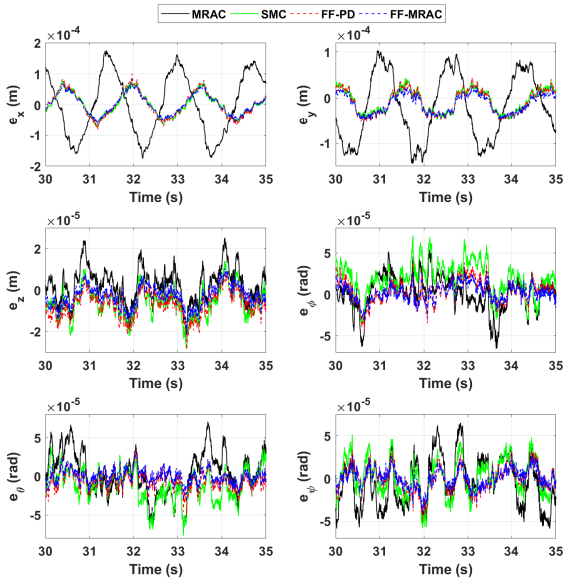

Figure 6: Evolution versus time of the Cartesian tracking errors (Scenario 1).

4.2.2. Scenario 2: Robustness towards payload changes

The evolution of the tracking errors for this scenario, involving a 200 kg payload, are plotted in **Figures 10** and **11**. To highlight the difference between the implemented controllers, the plot has been zoomed in to cover the time span between 15 and 20 seconds. As the previous scenario, the proposed solution improves the tracking performance,

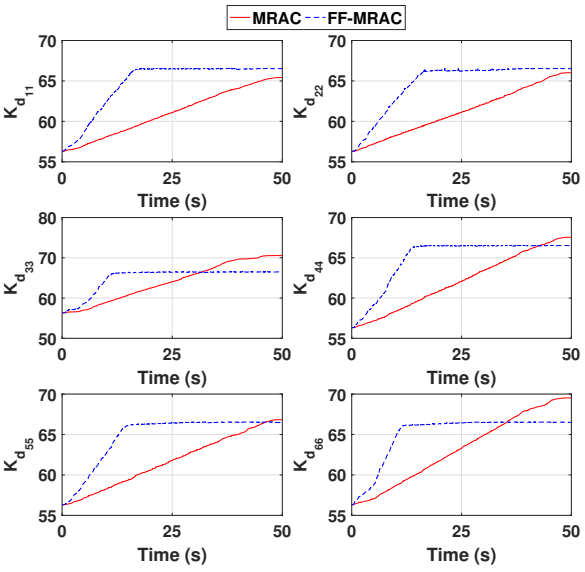

Figure 7: Evolution versus time of the derivative feedback gains (Scenario 1).

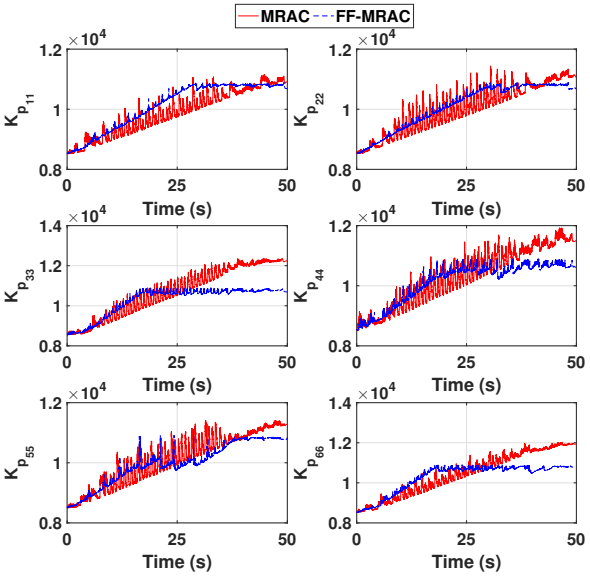

Figure 8: Evolution versus time of the proportional feedback gains (Scenario 1).

with a limited degradation with respect to the nominal scenario. By designing MRAC-based adaptive feedback gains with model-based dynamics compensation, a better tracking performance is obtained. This enhancement is also observed even when the feedforward term does not consider the additional payload. Despite some degradation due to uncertainties, the proposed controller consistently yields improved outcomes, as it is highlighted from the summarized RMSE values in **Tables** 4, 5 and 6. The evolution of the adaptive feedback gains is depicted in **Figures** 12, and 13.

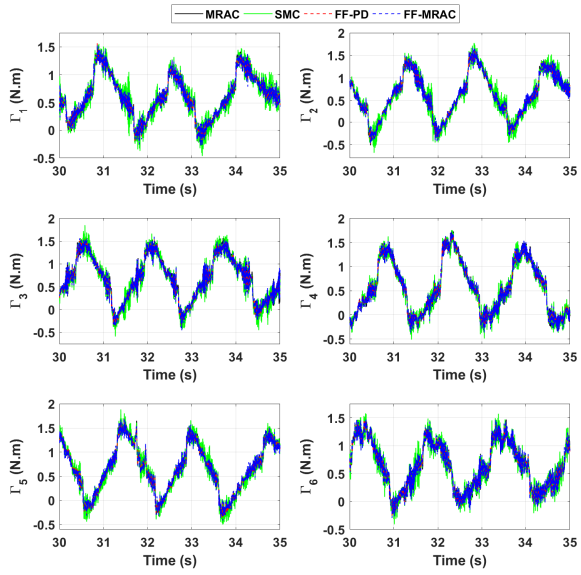

Figure 9: Evolution versus time of the control input torques (Scenario 1).

Table 3
Scenario 1: Tracking performance evaluation with the calculated improvements.

Controllers	$RMS_q\,(\mu m)$	$RMS_t\,(\mu m)$	$RMS_r\,(mdeg)$
MRAC	116.4157	103.1585	3.5695
SMC	58.4582	33.5699	2.62608
FF-PD	49.4263	36.0550	1.6746
FF-MRAC	42.3012	29.6635	1.3768
Imp./MRAC	63.66 %	71.24 %	61.42 %
Imp./SMC	27.64 %	11.63 %	47.57 %
Imp./FF-PD	14.41 %	17.72 %	17.78 %

Thanks to the projection operator, even in the presence of uncertainties, the proposed controller feedback gains do not exceed their maximum values. On the contrary, the MRAC controller might need high feedback gains to minimize the tracking errors, which can inadvertently result in vibrations and oscillations in the input torque and tracking errors. The evolution of the generated control input torques is depicted in **Figure** 14. Once again, the plot has been zoomed in, this time within the interval $[15\,s, 20\,s]$ for readability purpose. The obtained torques remain within their admissible range, and the energy consumption remains nearly identical among the various controllers.

4.2.3. Scenario 3: Robustness towards velocity changes

The resulting tracking errors from the second robustness test involving high velocities are depicted in **Figures** 15 and 16. To highlight the difference between the implemented controllers, the plot has been zoomed in within the range of $[20\,s, 25\,s]$. The effectiveness of the proposed model-based feedforward term in compensating for dynamic variations

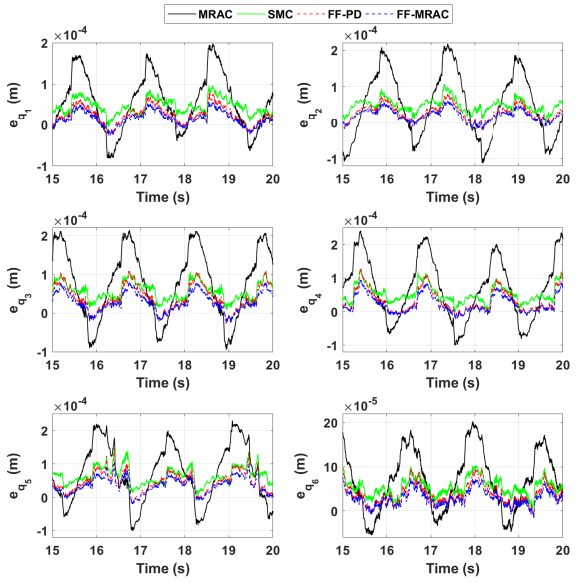

Figure 10: Evolution versus time of the joint tracking errors (Scenario 2 – 200 kg).

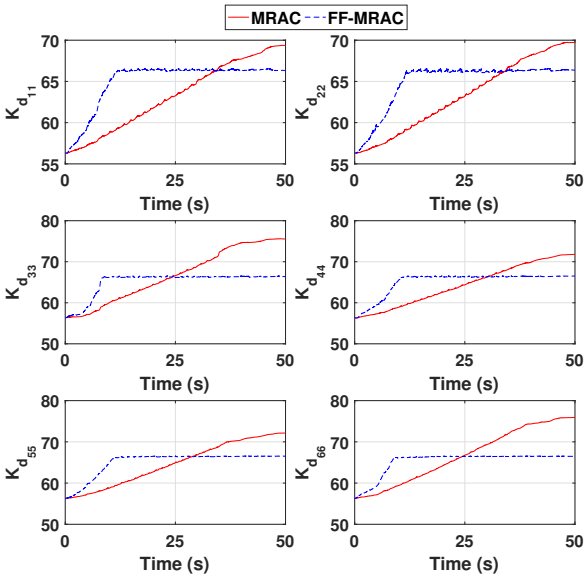

Figure 12: Evolution versus time of the derivative feedback gains (Scenario 2 – 200 kg).

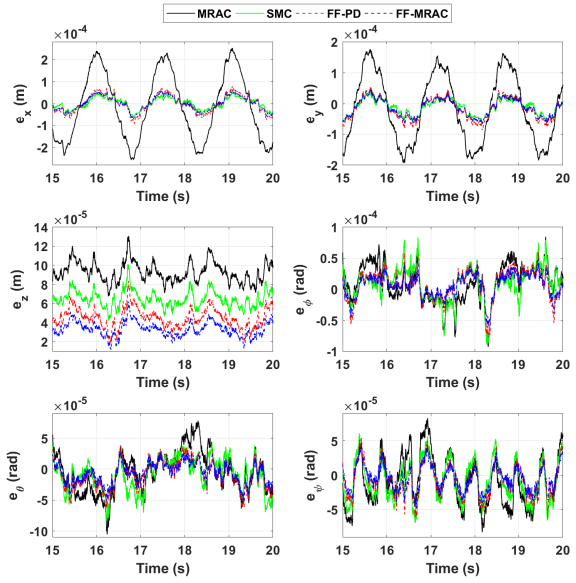

Figure 11: Evolution versus time of the Cartesian tracking errors (Scenario 2 – 200 kg).

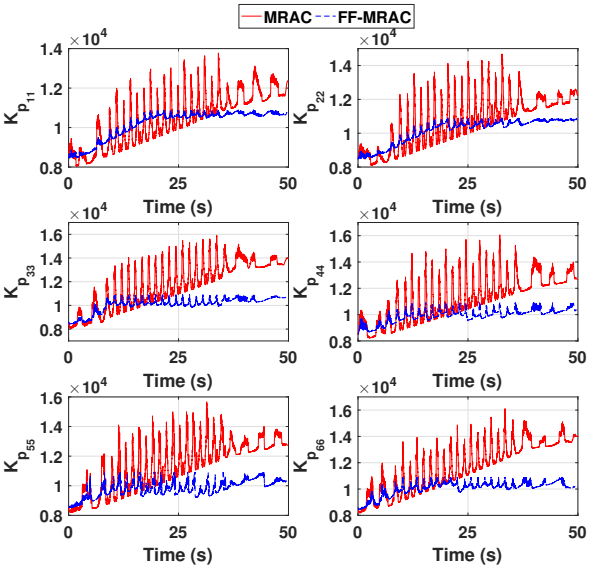

Figure 13: Evolution versus time of the proportional feedback gains (Scenario 2 – 200 kg).

is rather evident. This stands in contrast to the computed torque formulation, where the feedback signals introduce measurement noise into the control loop. Moreover, the incorporation of the adaptation rules based on reference model dynamics, used to update the feedback gains, enhances the tracking performance of the proposed controller. This improvement is corroborated by the calculation of RMSEs, where the results are summarized in **Table 7**. Besides, it is worth noting that since the reference input for ψ is zero, then dynamic compensation for this coordinate is absent, resulting in practically equivalent performances for all the controllers, as shown in **Figure 16**. The evolution of the adaptive feedback gains is depicted in **Figures 17**, **18**. As the previous scenarios, the inclusion of a projection operator ensures that the proposed controller's feedback gains remain within their admissible limits. In **Figure 19**, the generated control input torques are displayed, with the plot zoomed in within the interval $[20\,s, 25\,s]$ for improved visual clarity.

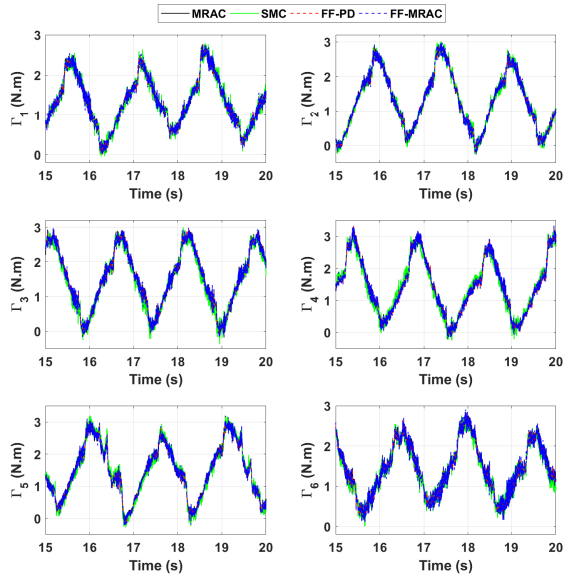

Figure 14: Evolution versus time of the control input torques (Scenario 2 – 200 kg).

Table 4
Scenario 2 (100 kg): Tracking performance evaluation with the calculated improvements.

Controllers	$RMS_q(\mu m)$	$RMS_t(\mu m)$	$RMS_r(mdeg)$
MRAC	154.4285	129.0201	3.7190
SMC	78.7294	40.1313	3.0186
FF-PD	63.8796	41.4154	1.6787
FF-MRAC	52.3329	35.8561	1.3932
Imp./MRAC	66.11 %	72.05 %	62.54 %
Imp./SMC	33.52 %	10.15 %	53.84 %
Imp./FF-PD	18.07 %	13.42 %	17.00 %

Table 5
Scenario 2 (150 kg): Tracking performance evaluation with the calculated improvements.

Controllers	$RMS_q(\mu m)$	$RMS_t(\mu m)$	$RMS_r(mdeg)$
MRAC	186.5788	149.5045	4.0607
SMC	104.9665	52.2725	3.3477
FF-PD	85.8536	50.0791	2.0763
FF-MRAC	68.3133	39.7636	1.6221
Imp./MRAC	63.38 %	73.40 %	60.05 %
Imp./SMC	34.91 %	23.93 %	51.54 %
Imp./FF-PD	20.43 %	20.59 %	21.87 %

Throughout this real-time experiment, the generated torques remain consistently within their permissible ranges, while energy consumption remains almost identical for the various implemented controllers.

Table 6
Scenario 2 (200 kg): Tracking performance evaluation with the calculated improvements.

Controllers	$RMS_q(\mu m)$	$RMS_t(\mu m)$	$RMS_r(mdeg)$
MRAC	224.9295	170.9349	4.3934
SMC	140.4936	71.9010	3.7672
FF-PD	103.3227	65.8095	2.6336
FF-MRAC	79.6162	51.8343	2.1131
Imp./MRAC	64.60 %	69.67 %	51.90 %
Imp./SMC	43.33 %	27.90 %	43.91 %
Imp./FF-PD	22.94 %	21.23 %	19.76 %

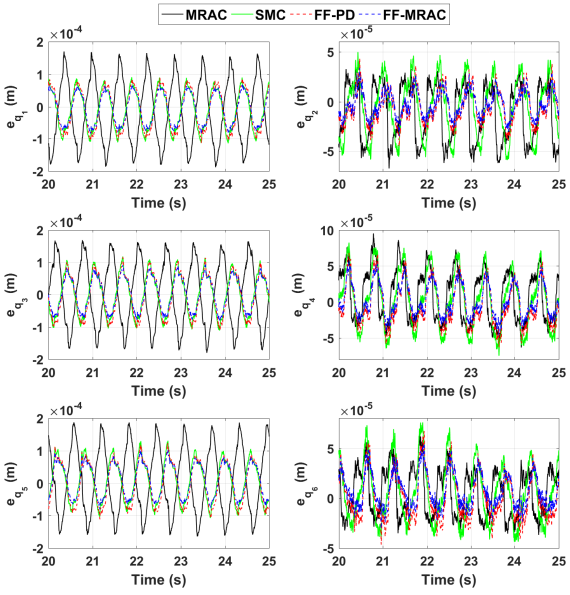

Figure 15: Evolution versus time of the joint tracking errors (Scenario 3 – 1.6 Hz).

5. Conclusion and Future Work

In this paper, a novel augmented MRAC approach for PKMs is proposed, including a feedforward dynamic term and enhanced adaptation gain rules. Furthermore, the stability analysis of the resulting closed-loop system is provided. The proposed control scheme has been validated through real-time experiments on FOEHN parallel robot, demonstrating the effectiveness and the superiority of the proposed controller, particularly in terms of robustness towards uncertainties. As future work, it is planned to make the feedforward term adaptive, with a real-time estimation of the PKM dynamic parameters. Alternatively, the friction model can be enhanced by incorporating the Stribeck effect, along with a sensitivity study to evaluate how the MRAC adaptation efficiency is influenced by different friction models.

in order to compensate for larger uncertainties and further enhance the tracking performance.

Table 7
Scenario 3: Tracking performance evaluation with the calculated improvements.

Case	$f = 1.3\,Hz$			$f = 1.6\,Hz$		
Controllers	$RMS_q\,(\mu m)$	$RMS_t\,(\mu m)$	$RMS_r\,(mdeg)$	$RMS_q\,(\mu m)$	$RMS_t\,(\mu m)$	$RMS_r\,(mdeg)$
MRAC	139.6882	82.3290	7.7412	175.6005	111.1531	9.3685
SMC	91.5442	32.7780	5.9048	115.9243	45.7528	7.8002
FF-PD	76.9159	34.5941	4.9163	110.1537	50.4053	7.0608
FF-MRAC	64.1976	29.2155	4.0883	88.6642	41.3279	5.6377
Imp./MRAC	54.04 %	64.51 %	47.18 %	49.51 %	62.82 %	39.82 %
Imp./SMC	29.87 %	10.86 %	30.76 %	23.51%	09.67 %	27.72 %
Imp./FF-PD	16.53 %	15.54 %	16.84 %	19.51 %	18.01 %	20.15 %

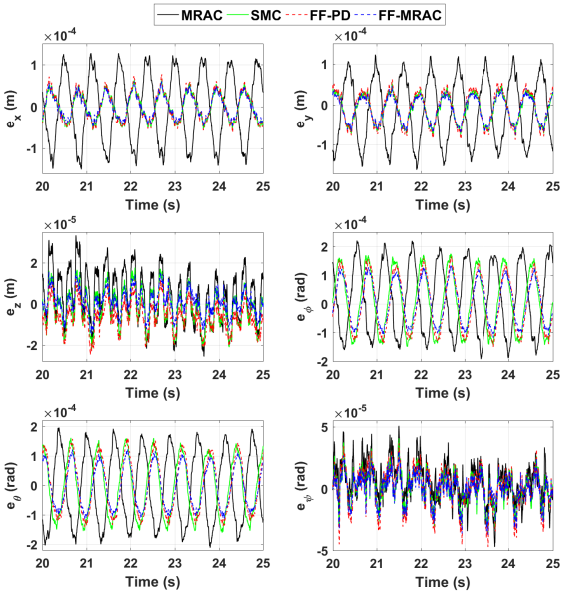

Figure 16: Evolution versus time of the Cartesian tracking errors (Scenario 3 – 1.6 Hz).

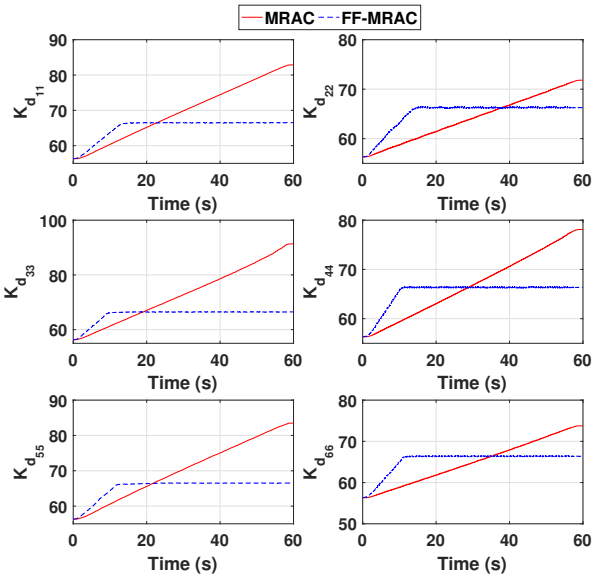

Figure 17: Evolution versus time of the derivative feedback gains (Scenario 3 – 1.6 Hz).

Acknowledgment

This study was supported by the SYMETRIE company, within the CIFRE (Convention Industrielle de Formation par la Recherche) research project, Grant N° 2021/0900.

References

[1] J. Wu, B. Zhang, L. Wang, G. Yu, An iterative learning method for realizing accurate dynamic feedforward control of an industrial hybrid robot, Science China Technological Sciences 64 (2021) 1177–1188.

[2] M. Escorcia-Hernández, Jonatan, A. Chemori, H. Aguilar-Sierra, Adaptive rise feedback control for robotized machining with pkms: Design and real-time experiments, IEEE Transactions on Control Systems Technology 31 (2023) 39–54.

[3] S. Keshtkar, A. S. Poznyak, E. Hernandez, A. Oropeza, Adaptive sliding-mode controller based on the "super-twist" state observer for control of the stewart platform, Automation and Remote Control 78 (2017) 1218–1233.

[4] W. Dong, Z. Du, Y. Xiao, X. Chen, Development of a parallel kinematic motion simulator platform, Mechatronics 23 (2013) 154–161.

[5] H. D. Taghirad, Parallel robots: mechanics and control, CRC press, 2013.

[6] F. Zaccaria, E. Idà, S. Briot, Design and experimental equilibrium stability assessment of a rfrfr continuum parallel robot, Mechatronics 95 (2023) 103064.

[7] J. Wu, G. Yu, Y. Gao, L. Wang, Mechatronics modeling and vibration analysis of a 2-dof parallel manipulator in a 5-dof hybrid machine tool, Mechanism and Machine Theory 121 (2018) 430–445.

[8] Z. Zhang, G. Xie, Z. Shao, C. Gosselin, Kinematic calibration of cable-driven parallel robots considering the pulley kinematics, Mechanism and Machine Theory 169 (2022) 104648.

[9] E. Picard, F. Plestan, E. Tahoumi, F. Claveau, S. Caro, Control strategies for a cable-driven parallel robot with varying payload information, Mechatronics 79 (2021) 102648.

[10] J. Piao, M.-C. Kim, E.-S. Kim, C.-S. Kim, A self-adaptive inertia hybrid control of a fully constrained cable-driven parallel robot, IEEE Transactions on Automation Science and Engineering (2023) 1–11.

[11] V. Rosenzveig, S. Briot, P. Martinet, E. Özgür, N. Bouton, A method for simplifying the analysis of leg-based visual servoing of parallel robots, in: 2014 IEEE International Conference on Robotics and Automation (ICRA), 2014, pp. 5720–5727. doi:10.1109/ICRA.2014.6907700.

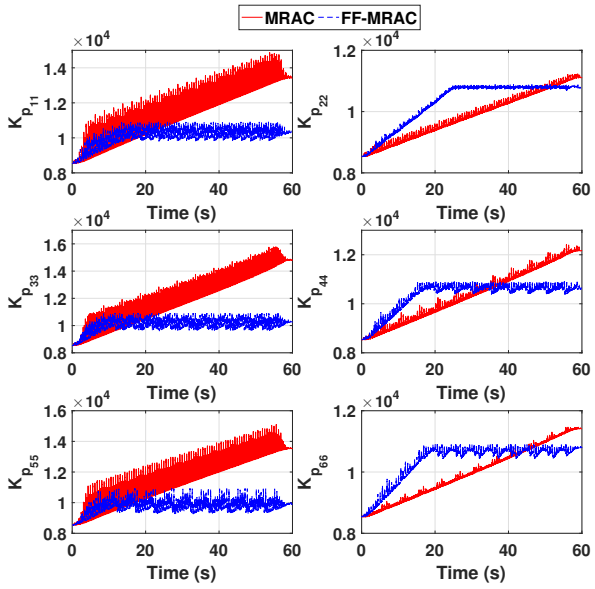

Figure 18: Evolution versus time of the proportional feedback gains (Scenario 3 – 1.6 Hz).

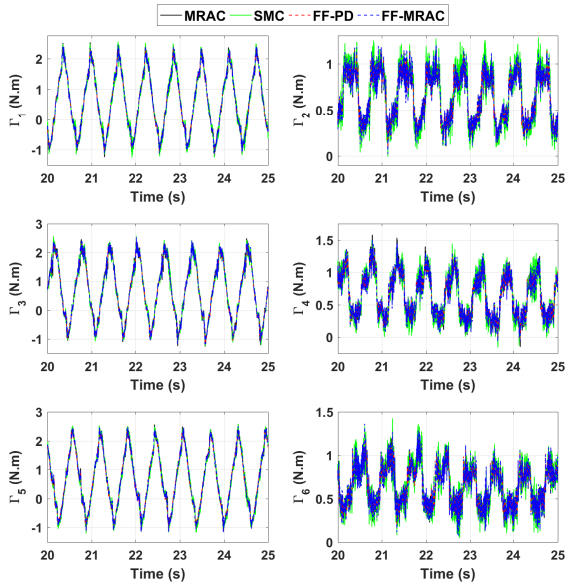

Figure 19: Evolution versus time of the control input torques (Scenario 3 – 1.6 Hz).

[12] A. Chemori, Control of complex robotic systems: Challenges, design and experiments, in: 2017 22nd International Conference on Methods and Models in Automation and Robotics (MMAR), IEEE, 2017, pp. 622–631.

[13] J. Wu, J. Wang, L. Wang, T. Li, Dynamics and control of a planar 3-dof parallel manipulator with actuation redundancy, Mechanism and Machine Theory 44 (2009) 835–849.

[14] F. Valero, M. Díaz-Rodríguez, M. Vallés, A. Besa, E. Bernabéu, A. Valera, Reconfiguration of a parallel kinematic manipulator with 2T2R motions for avoiding singularities through minimizing actuator forces, Mechatronics 69 (2020) 102382.

[15] S. Staicu, Dynamics of Parallel Robots, Springer, 2019.

[16] M. G. Villarreal-Cervantes, J. Alvarez-Gallegos, Off-line pid control tuning for a planar parallel robot using de variants, Expert Systems with Applications 64 (2016) 444–454.

[17] B. Zhou, Y. Wang, B. Zi, W. Zhu, Fuzzy adaptive whale optimization control algorithm for trajectory tracking of a cable-driven parallel robot, IEEE Transactions on Automation Science and Engineering (2023) 1–12.

[18] A. Al-Mayyahi, A. Aldair, C. Chatwin, Control of a 3-rrr planar parallel robot using fractional order pid controller, International Journal of Automation and Computing 17 (2020) 822–836.

[19] M. S. Ayas, E. Sahin, I. H. Altas, High order differential feedback controller design and implementation for a stewart platform, Journal of Vibration and Control 26 (2020) 976–988.

[20] H. Saied, A. Chemori, M. El Rafei, C. Francis, F. Pierrot, From non-model-based to model-based control of pkms: a comparative study, in: Mechanism, Machine, Robotics and Mechatronics Sciences, Springer, 2019, pp. 153–169.

[21] T. W. Seo, H. S. Kim, D. S. Kang, J. Kim, Gain-scheduled robust control of a novel 3-DOF micro parallel positioning platform via a dual stage servo system, Mechatronics 18 (2008) 495–505.

[22] S. M. Fazeli, A. Ameri, A. Molaei, M. A. Khosravi, M. Hassani, Dynamic model-free control approach for fully constrained cable-driven parallel robots: Prescribed control range, IEEE Transactions on Industrial Electronics (2023) 1–10.

[23] H. Saied, A. Chemori, M. Bouri, M. El Rafei, C. Francis, F. Pierrot, A new time-varying feedback rise control for second-order nonlinear mimo systems: theory and experiments, International Journal of Control 94 (2021) 2304–2317.

[24] K. V. Sancak, Z. Y. Bayraktaroglu, Nonlinear computed torque control of 6-dof parallel manipulators, International Journal of Control, Automation and Systems 20 (2022) 2297–2311.

[25] S. Xiaogang, Y. Zhao, L. Jin, P. Zhang, C. Chen, Dynamic feed-forward control in decoupling space for a four-degree-of-freedom parallel robot, International Journal of Advanced Robotic Systems 16 (2019) 172988141882045.

[26] W. Shang, S. Cong, Z. X. Li, S. L. Jiang, Augmented nonlinear pd controller for a redundantly actuated parallel manipulator, Advanced Robotics 23 (2009) 1725–1742.

[27] H. Saied, A. Chemori, M. Bouri, M. E. Rafei, C. Francis, Feedforward super-twisting sliding mode control for robotic manipulators: Application to pkms, IEEE Transactions on Robotics (2023) 1–18.

[28] M. Ye, G. Gao, J. Zhong, Finite-time stable robust sliding mode dynamic control for parallel robots, International Journal of Control, Automation and Systems 19 (2021).

[29] M. Barghandan, A. A. Pirmohamadi, S. Mobayen, A. Fekih, Optimal adaptive barrier-function super-twisting nonlinear global sliding mode scheme for trajectory tracking of parallel robots, Heliyon 9 (2023).

[30] B. Zhang, B. Deng, X. Gao, W. Shang, S. Cong, Design and implementation of fast terminal sliding mode control with synchronization error for cable-driven parallel robots, Mechanism and Machine Theory 182 (2023) 105228.

[31] R. Bordalba, J. M. Porta, L. Ros, A singularity-robust lqr controller for parallel robots, in: 2018 IEEE/RSJ International Conference on Intelligent Robots and Systems (IROS), 2018, pp. 270–276. doi:10.1109/IROS.2018.8594084.

[32] G. Chen, S. Hutchinson, F. Dellaert, Locally optimal estimation and control of cable driven parallel robots using time varying linear quadratic gaussian control, in: 2022 IEEE/RSJ International Conference on Intelligent Robots and Systems (IROS), 2022, pp. 7367–7374. doi:10.1109/IROS47612.2022.9981144.

[33] A. Chemori, R. Kouki, F. Bouani, A new fast nonlinear model predictive control of parallel manipulators: Design and experiments, Control Engineering Practice 130 (2023) 1105367.

[34] M. Ghafarian Tamizi, A. A. Ahmadi Kashani, F. Abed Azad, A. Kalhor, M. T. Masouleh, Experimental study on a novel simultaneous control and identification of a 3-dof delta robot using model reference adaptive control, European Journal of Control 67 (2022) 100715.

[35] M. R. J. Harandi, A. Hassani, M. I. Hosseini, H. D. Taghirad, Adaptive position feedback control of parallel robots in the presence of kinematics and dynamics uncertainties, IEEE Transactions on Automation Science and Engineering (2023) 1–11.

[36] C. C. Nguyen, S. S. Antrazi, Z.-L. Zhou, C. E. Campbell Jr., Adaptive control of a stewart platform-based manipulator, Journal of Robotic Systems 10 (1993) 541–555.

[37] N. T. Nguyen, Model-reference adaptive control, Springer, 2018.

[38] X. Dai, S. Song, W. Xu, Z. Huang, D. Gong, Modal space neural network compensation control for gough-stewart robot with uncertain load, Neurocomputing 449 (2021) 245–257.

[39] M. Zhu, C. Huang, S. Song, S. Xu, D. Gong, Vision-admittance-based adaptive rbfnn control with a smc robust compensator for collaborative parallel robots, Journal of the Franklin Institute 361 (2024) 106538.

[40] B. Dasgupta, T. Mruthyunjaya, The stewart platform manipulator: a review, Mechanism and Machine Theory 35 (2000) 15–40.

[41] J. Gallardo-Alvarado, Kinematic analysis of parallel manipulators by algebraic screw theory, Springer, 2016.

[42] J.-P. Merlet, Parallel robots, volume 128, Springer Science & Business Media, 2006.

[43] H. Saied, A. Chemori, M. E. Rafei, C. Francis, F. Pierret, Actuator and friction dynamics formulation in control of pkms: From design to real-time experiments, in: 2018 IEEE/RSJ International Conference on Intelligent Robots and Systems (IROS), 2018, pp. 5634–5639. doi:10.1109/IROS.2018.8594329.

[44] W. Khalil, E. Dombre, Modeling identification and control of robots, CRC Press, 2002.

[45] N. Hovakimyan, C. Cao, $\mathcal{L}_1$ Adaptive Control Theory: Guaranteed Robustness with Fast Adaptation, SIAM, 2010.

[46] D. Zhang, B. Wei, A review on model reference adaptive control of robotic manipulators, Annual Reviews in Control 43 (2017) 188–198.